

Predictive modeling of NSTX discharges with the updated multi-mode anomalous transport module

T. Rafiq^{1,*} , C. Wilson¹ , C. Clauser^{1,a} , E. Schuster¹ , J. Weiland¹ , J. Anderson² , S.M. Kaye³ , A. Pankin³ , B.P. LeBlanc³  and R.E. Bell³ 

¹ Lehigh University, Bethlehem, PA, United States of America

² Chalmers University of Technology, Gothenburg, Sweden

³ Princeton Plasma Physics Laboratory, Princeton, NJ, United States of America

E-mail: rafiq@lehigh.edu

Received 14 January 2024, revised 17 April 2024

Accepted for publication 17 May 2024

Published 3 June 2024



CrossMark

Abstract

The objective of this study is twofold: firstly, to demonstrate the consistency between the anomalous transport results produced by updated Multi-Mode Model (MMM) version 9.0.4 and those obtained through gyrokinetic simulations; and secondly, to showcase MMM's ability to predict electron and ion temperature profiles in low aspect ratio, high beta NSTX discharges. MMM encompasses a range of transport mechanisms driven by electron and ion temperature gradients, trapped electrons, kinetic ballooning, peeling, microtearing, and drift resistive inertial ballooning modes. These modes within MMM are being verified through corresponding gyrokinetic results. The modes that potentially contribute to ion thermal transport are stable in MMM, aligning with both experimental data and findings from linear CGYRO simulations. The isotope effects on these modes are also studied and higher mass is found to be stabilizing, consistent with the experimental trend. The electron thermal power across the flux surface is computed within MMM and compared to experimental measurements and nonlinear CGYRO simulation results. Specifically, the electron temperature gradient modes (ETGM) within MMM account for 2.0 MW of thermal power, consistent with experimental findings. It is noteworthy that the ETGM model requires approximately 5.0 ms of computation time on a standard desktop, while nonlinear CGYRO simulations necessitate 8.0 h on 8 K cores. MMM proves to be highly computationally efficient, a crucial attribute for various applications, including real-time control, tokamak scenario optimization, and uncertainty quantification of experimental data.

Keywords: transport, NSTX, predictive simulation, tokamak, multi-mode module

(Some figures may appear in colour only in the online journal)

^a Present address: Massachusetts Institute of Technology, Cambridge, MA, United States of America.

* Author to whom any correspondence should be addressed.



Original Content from this work may be used under the terms of the [Creative Commons Attribution 4.0 licence](https://creativecommons.org/licenses/by/4.0/). Any further distribution of this work must maintain attribution to the author(s) and the title of the work, journal citation and DOI.

1. Introduction

Predicting time-dependent electron and ion temperature profiles in the National Spherical Torus Experiment (NSTX) presents a challenge due to its low aspect ratio and high beta discharges, unlike conventional fusion devices with larger aspect ratios and lower beta discharges. Previously, an earlier version of the Multi-Mode Model (MMM) [1] was used in the integrated modeling code TRANSP [2] to successfully predict plasma profiles in conventional devices such as JET, DIII-D, EAST, and KSTAR [3]. The updated version, MMM 9.0.4, is now incorporated into TRANSP to demonstrate the consistency of MMM results with gyrokinetic simulations and its capability to predict electron and ion temperature profiles in NSTX discharges [4].

In the realm of gyrokinetic simulations, it is common practice to simulate only a few tens of microseconds of plasma time, which requires tens to hundreds of hours of computer simulation time before turbulence stabilizes into a quasi-steady state. Simulating processes on the timescale of a tokamak discharge, which can span tens to hundreds of seconds, necessitates the inclusion of physics-based fluid transport modules to accurately describe turbulence-driven anomalous transport.

The physics-based MMM is a multi-species, multi-fluid, multi-mode anomalous transport model that calculates electron and ion thermal transport, electron particle transport, impurity transport, and toroidal and poloidal momentum transport in tokamak discharges. The MMM comprises four components: (i) the Weiland model for transport driven by ion temperature gradient (ITG), trapped electrons (TE), kinetic ballooning (KB), peeling, and high mode number MHD modes [5]; (ii) a new model of electromagnetic electron temperature gradient mode (ETGM) for electron thermal transport [6]; (iii) an updated model of microtearing mode (MTM) for transport driven by electron temperature gradients in both the collisionless and collisionality regimes in the presence of perturbations of the magnetic flux surfaces [7]; and (iv) an updated model for the drift resistive inertial ballooning mode (DRIBM) for transport driven by gradients, electron inertial effects, and inductive effects [8]. Numerous upgrades have been implemented to enhance the precision, consistency, speed, and physical basis of these MMM components. These improvements are crucial not only for the NSTX/NSTX-U but also for the development of reactor concepts based on spherical tokamaks.

Aside from drift modes, MMM is characterized by the exclusive presence of high mode number MHD modes, where the ballooning mode formalism is applicable, with the absence of low MHD mode numbers. Furthermore, MMM currently does not incorporate considerations for fast particle-induced transport and the physics of multi-scale interactions. Consequently, MMM may not accurately predict plasma profiles for tokamak discharges featuring low mode number MHD activity, significant fast particle transport, and multi-scale interaction physics. A forthcoming development involves the incorporation of a fast particle model into MMM for future simulations [9].

The structure of this paper is outlined as follows: section 2 presents the NSTX parameters pertaining to discharges with both high and low collisionality. Section 3 analyzes the real frequency, growth rate, fluxes, and diffusivities of standalone MMM under both flow shear on and off conditions. The discussion also encompasses the impact of isotopes on unstable modes. Section 4 presents the results obtained using the MMM and compares them to the results generated by CGYRO [10]. Section 5 presents the predicted temporal profiles of NSTX discharges, specifically focusing on low and high collisionality discharges. Section 6 provides a conclusion of the results obtained from the MMM analysis, as well as a comparison of these results with those obtained from gyrokinetic simulations and experimental observations.

2. NSTX low and high collisionality discharges

The NSTX high collisionality discharge (120968) and the low collisionality discharge (120982), both NBI-heated H-mode discharges, are considered for the calculation of modes present in MMM. The NBI power of 4.1 MW is injected in both low and high collisionality cases. The NBI power deposited on ions and electrons and beam current are calculated using the NUBEAM module [11]. In the low collisionality case, the total current and magnetic field strength are 1.12 MA and 0.55 T, respectively, whereas in the high collisionality case, they are 0.71 MA and 0.35 T, respectively. The q_{95} values for both discharges are around 11. Both shots exhibit a dW/dt that is 10% or less of the heating power, with characteristic time-scales for the stored energy (W) change that are a factor of 10 or so greater than the energy confinement times. While shot 120982 appears to be relatively stable, shot 120968 shows some variability. Therefore, from a confinement standpoint, shot 120982 can be considered relatively stationary due to its stable and consistent behavior, whereas shot 120968 may not be considered entirely stationary due to the observed variability in stored energy over time.

As can be seen in figure 1, the core input profiles, such as temperature, density, safety factor, and elongation, differ between both discharges, resulting in varying gradients. The profiles are plotted versus radial coordinate, r , from the magnetic axis to 80% of the plasma minor radius a . The ‘ears’ in the electron density characteristic of NSTX H-modes are located around $r/a \sim 0.8$. These ‘ears’ indicate an electron density buildup at the plasma boundary due to carbon fueling of the edge. The effective electron beta, $\mathbf{E} \times \mathbf{B}$ shear, and collision frequency are plotted in figure 2, highlighting differences in the profiles. These profile variations will impact the stability of the modes, as well as thermal, particle, and momentum fluxes and diffusivities. The $\mathbf{E} \times \mathbf{B}$ shearing rate was inferred from the data and found to be larger in the low collisionality discharge than in the high collisionality discharge. An in-depth analysis to determine the reason for the stronger rotation in the low collisionality discharge has not yet been conducted. However, it appears that the beam configuration may have contributed to this phenomenon. The measured toroidal rotation frequency (ω_ϕ) can be seen in figure 3.

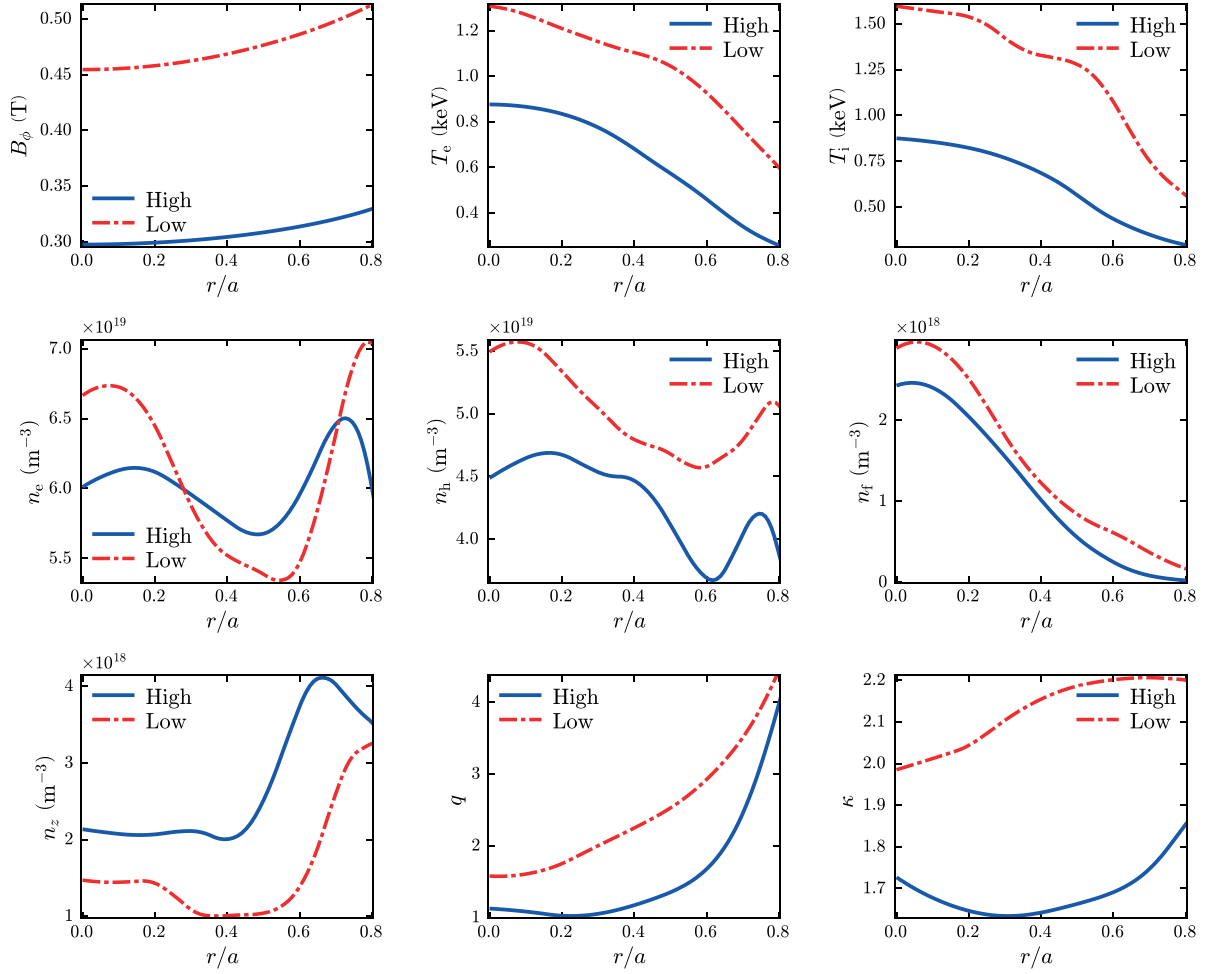


Figure 1. Parameters for high collisionality discharge 120968 at $t = 0.56$ s and low collisionality discharge 120982 at $t = 0.62$ s, including toroidal magnetic field (B_ϕ), electron temperature (T_e), ion temperature (T_i), electron density (n_e), hydrogenic species density (n_h , deuterium, by default), fast ion density (n_f), impurity density (n_z), safety factor (q), and elongation (κ).

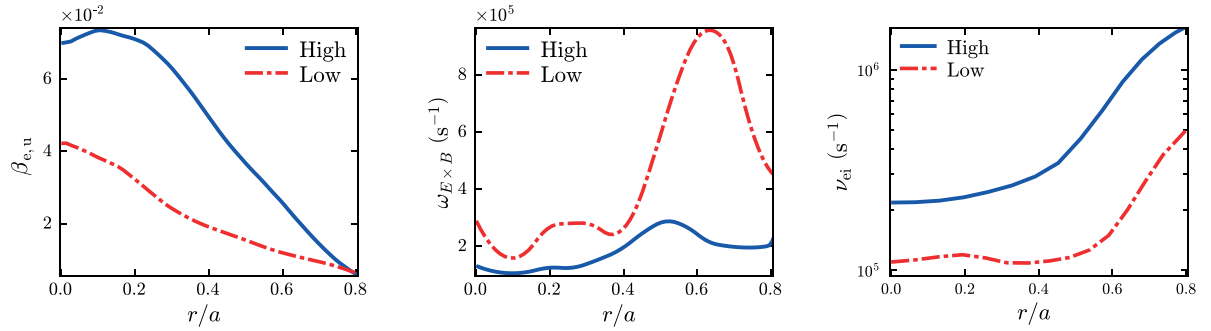


Figure 2. The effective electron beta ($\beta_{e,u}$), $\mathbf{E} \times \mathbf{B}$ flow shear ($\omega_{E \times B}$), and electron-ion collision frequency (ν_{ei}) are shown for high and low collisionality discharges.

In figure 3, we also present the normalized electron temperature gradient (g_{T_e}), normalized ITG (g_{T_i}), magnetic shear (s), normalized electron density gradient (g_{n_e}), and the normalized impurity density (g_{n_z}) for both high and low collisionality NSTX discharges. The normalized gradients used by the MMM follow the format

$$g_y = -\frac{R}{y} \frac{dy}{dr},$$

where g_y is the normalized gradient for some variable $y > 0$, R is the major radius, and r is the minor radius of the plasma.

3. Numerical results obtained using standalone MMM

The modes present in low and high collisionality discharges are shown below, both with and without the $\mathbf{E} \times \mathbf{B}$ flow shear

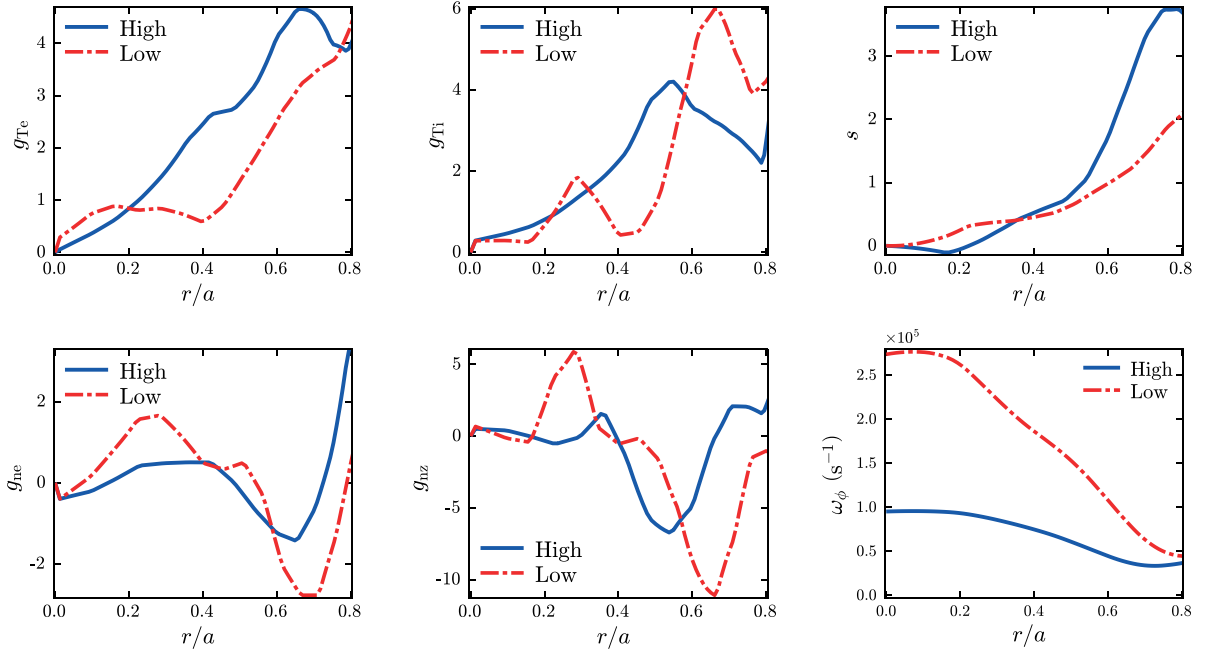


Figure 3. Normalized electron temperature gradient (g_{Te}), normalized ion temperature gradient (g_{Ti}), magnetic shear (s), normalized electron density gradient (g_{ne}), normalized impurity density (g_{nz}), and the toroidal rotation frequency are plotted in high and low collisionality NSTX discharges.

effect, in order to determine the types of modes that are present, stabilized by flow shear, or have survived. The effects of isotopes on the growth rate of modes are also determined. Note that standalone MMM utilizes input configurations shown in figure 1, forming the basis for numerical results. The information in figure 1 is a key reference for understanding conditions and settings in MMM simulations and analyses.

3.1. Results for low and high collisionality without the flow shear effect

The growth rate and frequency of ITG/TEM/KBM ($\gamma_{i,w20}$, $\omega_{i,w20}$), ETGM (γ_{etgm} , ω_{etgm}), MTM (γ_{mtm} , ω_{mtm}), and DRIBM (γ_{dbm} , ω_{dbm}) in the absence of flow shear are presented in figure 4 for high and low collisionality discharges. Note that $k_\theta \rho_s$ is not fixed at each surface; instead, a $k_\theta \rho_s$ scan is performed to determine the most unstable mode. Here, k_θ represents the poloidal wave vector, and ρ_s denotes the ion Larmor radius.

ITG/TEM/KBM instability is observed in both discharges, with these modes typically manifesting in the ion direction (negative ω). Additionally, these modes show a strong correlation with variations in the ITG within the plasma. It's noteworthy that these ITG/TEM/KBM modes have the potential to significantly influence ion thermal transport. However, in NSTX discharges, the primary mechanism governing ion thermal transport is neoclassical. This implies that neoclassical mechanisms, rather than ITG/TEM/KBM modes, primarily dictate ion thermal energy transport within the plasma in NSTX discharges. An intriguing aspect to consider is

the potential impact of flow shear on the stability of these ITG/TEM/KBM modes, which will be explored in the next subsection.

The instability associated with ETGM is electron-directional and linked to the electron temperature gradient within the plasma. ETGM growth rates are larger in high collisionality discharge due to the significant electron temperature gradient compared to low collisionality discharge. ETGMs exhibit significantly higher growth rates than flow shear, although flow shear can mitigate their adverse effects on plasma confinement. Nevertheless, these modes persist even in the presence of flow shear and contribute to electron thermal transport. ETGMs are identified as the most unstable among all instabilities in flow shear-off conditions and are likely to play a pivotal role in electron thermal transport in both low and high collisionality NSTX discharges.

MTMs, which rotate in the electron direction, are driven by gradients in electron temperature and density in the presence of collisionality, rendering them unstable. While in certain radial locations, the growth rate of MTM is higher in high collisionality cases, overall, the diffusivity attributed to MTM is expected to be greater in low collisionality cases throughout all radial positions. This phenomenon is due to the significantly elevated electron temperature in low collisionality cases, leading to a higher thermal velocity that amplifies transport effects. In the case of low collisionality discharges, MTM ion direction modes with a substantial growth rate are also observed in the region ($0.6 \leq r/a \leq 0.8$) with a negative electron density gradient (see g_{ne} in figure 3). MTMs display resilience in gyrokinetic simulations, even in the presence of

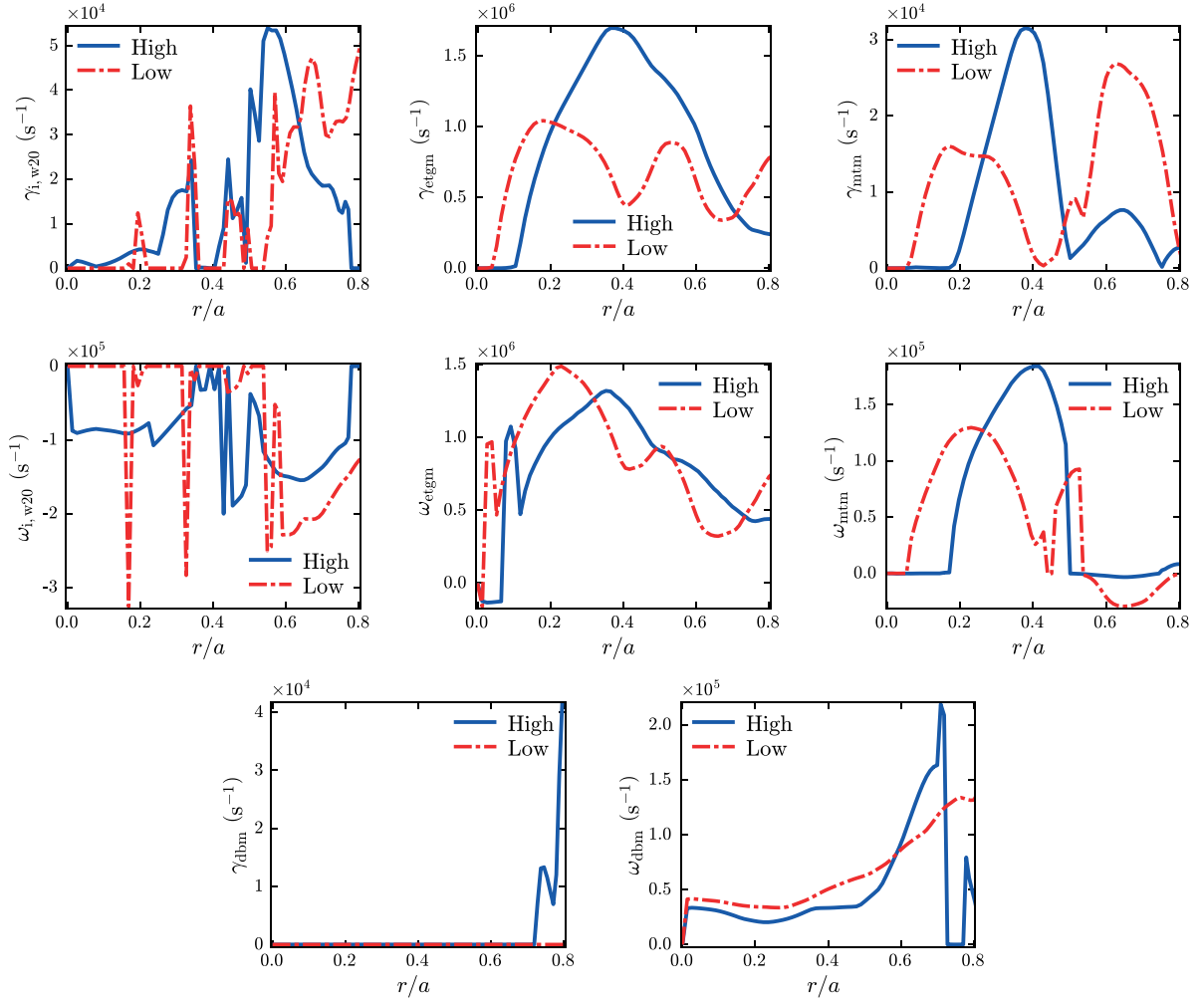


Figure 4. The growth rate and frequency of various instabilities, namely ITG/TEM/KBM ($\gamma_{i,w20}$, $\omega_{i,w20}$), ETGM (γ_{etgm} , ω_{etgm}), MTM (γ_{mtm} , ω_{mtm}), and DRIBM (γ_{dbm} , ω_{dbm}), are shown in high and low collisionality NSTX discharges in the absence of flow shear.

flow shear [10]. Therefore, the influence of flow shear will be disregarded, allowing these modes to maintain their original growth rate and contribute to electron thermal transport.

DRIBMs exhibit a complex instability resulting from density and temperature gradients, electrical resistivity, plasma inertia, and pressure gradients. In low collisionality discharges, these modes are stable, while in high collisionality discharges, they become unstable toward the edge of the plasma. They rotate in the electron's direction. However, the growth rate of the unstable mode in high collisionality discharges is relatively smaller than the flow shear. Consequently, it is expected that these modes will not significantly contribute to thermal and particle transport in flow shear-on conditions. CGYRO [12] simulations have provided valuable insights into the stability of plasma modes in NSTX discharges across a wide range of collisionality scenarios. Notably, these simulations have shown that TEM, MTM, ETGM, and KBM modes exhibit instability in both high and low collisionality discharges [10]. The observation that stands out is that, in both gyrokinetic and MMM simulations, the growth rate of ETGMs is the highest among all other unstable modes [13]. Additionally, electron thermal transport due to ETGMs

is also the most significant in both MMM and CGYRO simulations. This underscores the importance of gaining a comprehensive understanding and developing control strategies to improve plasma confinement and fusion device performance.

Figure 5 displays the total electron thermal flux (Γ_e) and ion thermal flux (Γ_i), electron particle flux (Γ_n), toroidal momentum flux (Γ_ϕ), poloidal momentum flux (Γ_θ), and impurity flux (Γ_z). Our observations reveal that in high collisionality discharges, there is a substantial electron thermal flux, primarily driven by a significant normalized electron temperature gradient and a high electron temperature. Conversely, in low collisionality scenarios, ion thermal flux dominates, primarily due to the pronounced normalized ITG and low magnetic shear. It's worth noting that the DRIBM instability in the edge region disrupts this trend in the high collisionality case, leading to distinct transport behavior. Furthermore, our analysis identifies a correlation between particle flux and g_{ne} . The particle flux is found to be large in the case of low collisionality discharge due to higher g_{ne} and lower magnetic shear compared to high collisionality discharge. This observation may be attributed to the destabilization of density gradient-driven

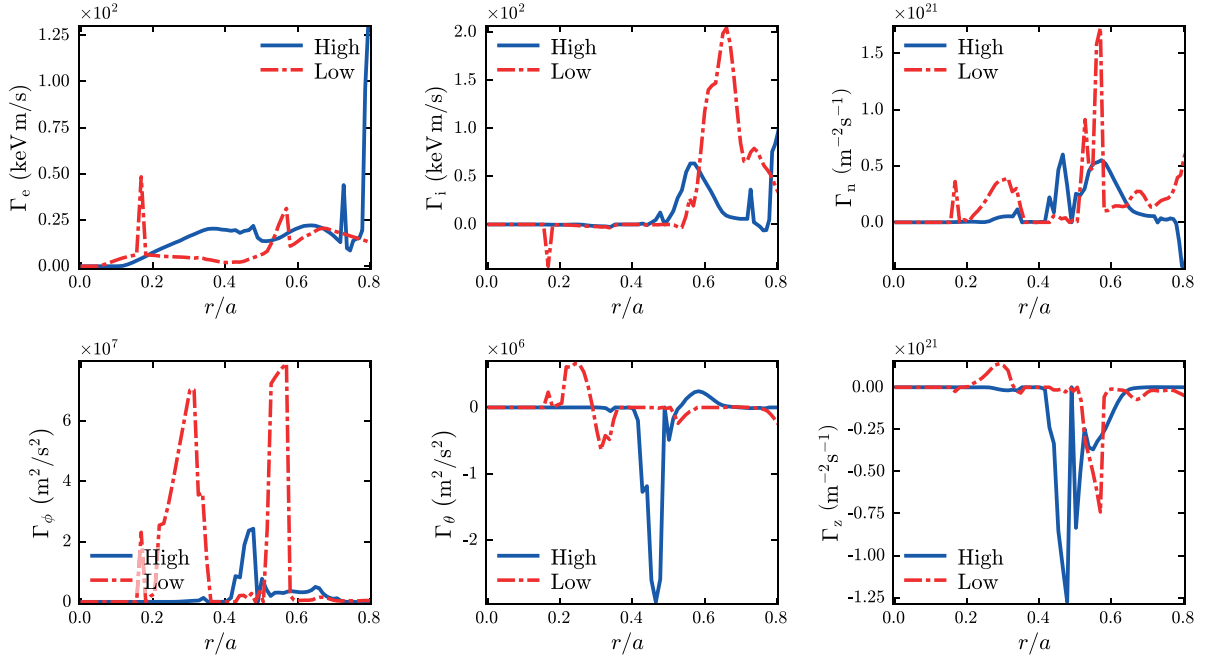


Figure 5. Total electron thermal flux (Γ_e) and ion thermal flux (Γ_i), particle flux (Γ_n), toroidal momentum flux (Γ_ϕ), poloidal momentum flux (Γ_θ), and impurity flux (Γ_z), under flow shear-off conditions, in high and low collisionality NSTX discharges.

TEM modes. Note that the particle flux around $r/a = 0.6$ is positive because the particle diffusivity and the corresponding gradient are negative, which makes the particle flux positive. Moreover, the occurrence of outward particle flux with varying signs of the density gradient is not uncommon. The flux spikes just after the gradient crosses zero, not where it crosses zero. These spikes are consistent with regions where the diffusivity is large and the gradient is non-zero. It is worth noting that the particle flux and particle pinch were previously compared with experimental results from both Tore Supra and EAST using the same model [14]. We also have had success in predicting the density profile in DIII-D discharges [3].

Toroidal momentum flux is notably associated with the g_{Ti} , while poloidal momentum flux exhibits prominence in regions characterized by substantial pressure gradients. Notably, impurity particle flux exhibits a close relationship with the g_{nz} , with evident impurity pinch effects manifesting in regions marked by negative values of g_{nz} . This investigation unveils the intricate relationships between various gradient parameters and transport phenomena within fusion devices, shedding light on the underlying physics that govern these complex interactions. These findings contribute to our fundamental understanding of plasma behavior and hold promise for optimizing fusion device performance and mitigating undesirable transport effects.

3.2. Results for low and high collisionality with the flow shear effect

The presence of $\mathbf{E} \times \mathbf{B}$ flow shear ($\omega_{E \times B}$) plays a crucial role in stabilizing or mitigating instabilities. In our numerical results, we take its effects into account. Instabilities like ITG/TEM/DRIBM/KBM, which contribute to ion thermal,

particle, and momentum transport, are found to be stabilized by $\omega_{E \times B}$. As a result, we anticipate that the confinement region in NSTX discharges under consideration will not exhibit anomalous ion thermal, particle, or momentum transport. Instead, the observed transports will follow neoclassical behavior. The finding of neoclassical ion thermal transport aligns with both CGYRO simulations and experimental results [10].

MTMs, being ion-scale modes, may initially appear to contribute to flow shear similarly to how ITG and TEM ion-scale modes contribute through toroidal and poloidal momentum transport. However, the fundamental distinction between electron transport induced by ITG/TEM and that by MTMs lies in the mechanisms involved. In ITG/TEM, electron thermal transport arises from $\mathbf{E} \times \mathbf{B}$ motion, whereas in MTMs, it is attributed to perturbations of the magnetic flux surfaces. As a result, momentum transport caused by the ion-scale MTM, which is unlikely to produce turbulence-driven rotation, is not considered in MMM's toroidal and poloidal momentum diffusivities.

In figure 6, we present the growth rates (γ_{etgm} , γ_{mtm}) of the ETGM and MTM modes, their corresponding electron thermal diffusivities ($\chi_{e,etgm}$, $\chi_{e,mtm}$), and total electron thermal diffusivity (χ_e) in the presence of flow shear ($\omega_{E \times B}$). The ETGM mode demonstrates resilience, indicating anomalous thermal electron transport in NSTX discharges, consistent with both CGYRO simulations and experimental findings. In contrast, CGYRO results show that MTM (γ_{mtm}) is unaffected by flow shear, so flow shear is not activated for MTMs [10]. ETGM (γ_{etgm}) is found to be less influenced by flow shear, except for $\hat{\rho} > 0.4$ in low collisionality cases where flow shear is substantial. The substantial growth rate of ETGM in high collisionality scenarios is primarily attributed to low flow shear and a

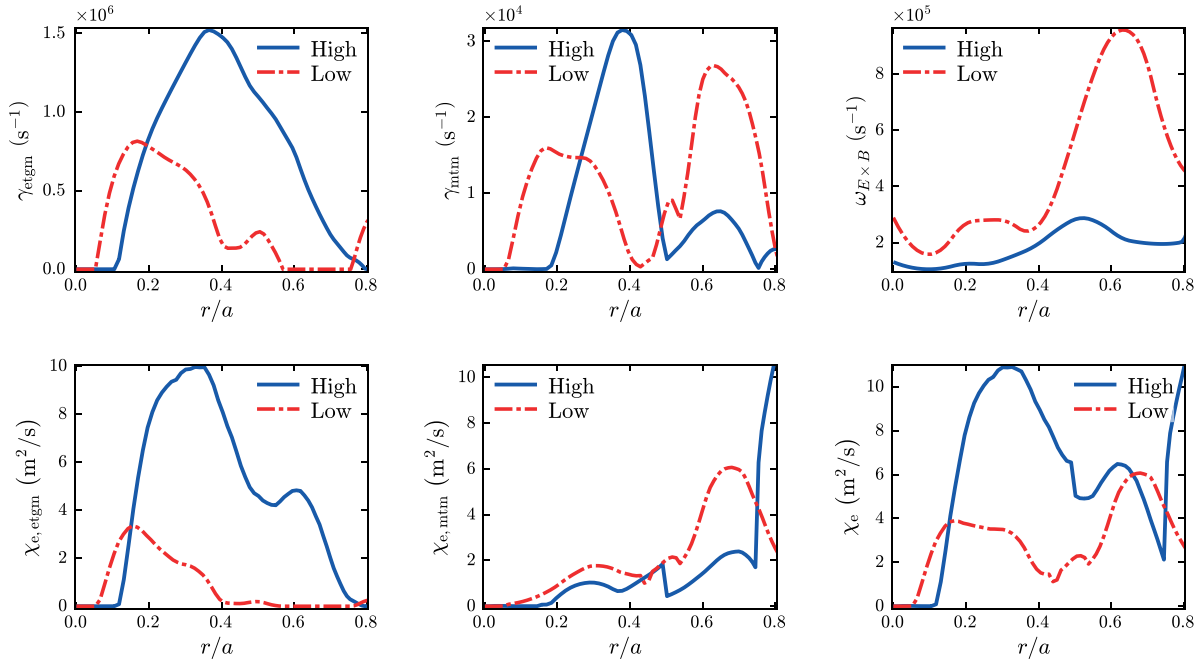


Figure 6. ETGM growth rate (γ_{etgm}), MTM growth rate (γ_{mtm}), and $\mathbf{E} \times \mathbf{B}$ flow shear ($\omega_{E \times B}$), ETGM electron thermal diffusivity ($\chi_{e,\text{etgm}}$), MTM electron thermal diffusivity ($\chi_{e,\text{mtm}}$), and total electron thermal diffusivity (χ_e) are plotted in high and low collisionality NSTX discharges.

significant electron temperature gradient. These factors also contribute to higher total electron thermal diffusivity in high collisionality discharges, as it is the sum of ETGM thermal diffusivity and MTM thermal diffusivity.

3.3. Effects of isotopes

In our study, we explore the effects of isotopes on the modes present in MMM for low and high collisionality discharges. Specifically, we examine the ITG/TEM growth rate ($\gamma_{i,w20}$), ETGM growth rate (γ_{etgm}), and MTM growth rate (γ_{mtm}), as displayed in figure 7 for hydrogen plasma (figures in the first row) and tritium plasma (figures in the second row) in both high and low collisionality discharges (these can also be compared to the deuterium results in figure 4).

Our findings reveal that these isotope effects have a stabilizing impact on ITG/TEM/KBM/MTM and DRIBM (not shown here) modes, while they are relatively insignificant for ETGM. This observation can be attributed to tritium's higher mass, which reduces the thermal velocity of tritium ions. Consequently, they are less susceptible to rapid motion caused by temperature-driven random particle motion, thereby reducing their contribution to turbulence and transport. Furthermore, the inclusion of ion viscosity in MMM plays a crucial role in replicating the experimental trend, where transport is observed to decrease with higher ion mass. The ion viscosity term is added to the ion energy perturbation equation, which is taken from Braginskii, and its role is to avoid fluid resonance [15]. It is noteworthy that ion viscosity is introduced as a replacement for the Landau fluid resonances observed in specific fluid models [16]. This indicates that the isotope scaling

mechanism functions within the framework of fluid closure, especially concerning the generation of zonal flows.

4. Comparison of ETGM to its corresponding CGYRO modes

The components of MMM undergo verification by comparing them to corresponding gyrokinetic results. Previously, the MTM model was verified against GYRO simulations, demonstrating close agreement between the MTM model in MMM and gyrokinetic results [17]. Here, we verify the newly developed electromagnetic ETGM model using CGYRO simulations, as illustrated in figure 8. Our findings show that the ETG-MMM model accurately reproduces the real frequency of ETGMs. Additionally, the magnitude of the most unstable mode in the $k_{\theta}\rho_s$ spectrum closely matches CGYRO results. Notably, the ETG-MMM mode stabilizes early in the $k_{\theta}\rho_s$ spectrum compared to the CGYRO model at both radii $r/a = 0.6$ and 0.7 . This difference can be due to the way FLR effects are included in the ETG-MMM model, where the norm of $\langle k_{\perp} \rangle$, based on a well-localized eigenfunction, is used. This discrepancy is addressed by calibrating the ETGM model's thermal diffusivity using NSTX discharges. Once calibrated, the model remains consistent and has not been adjusted across different tokamaks or between discharges. The electron thermal diffusivity, or electron thermal flux, is calculated using eigenvalues and eigenvectors. The eigenvalues determine the real frequency and growth rate of the mode, while the eigenvectors indicate the phase and magnitude of perturbed variables relative to each other. It's important to note that the eigenvectors used in the calculation of electron thermal

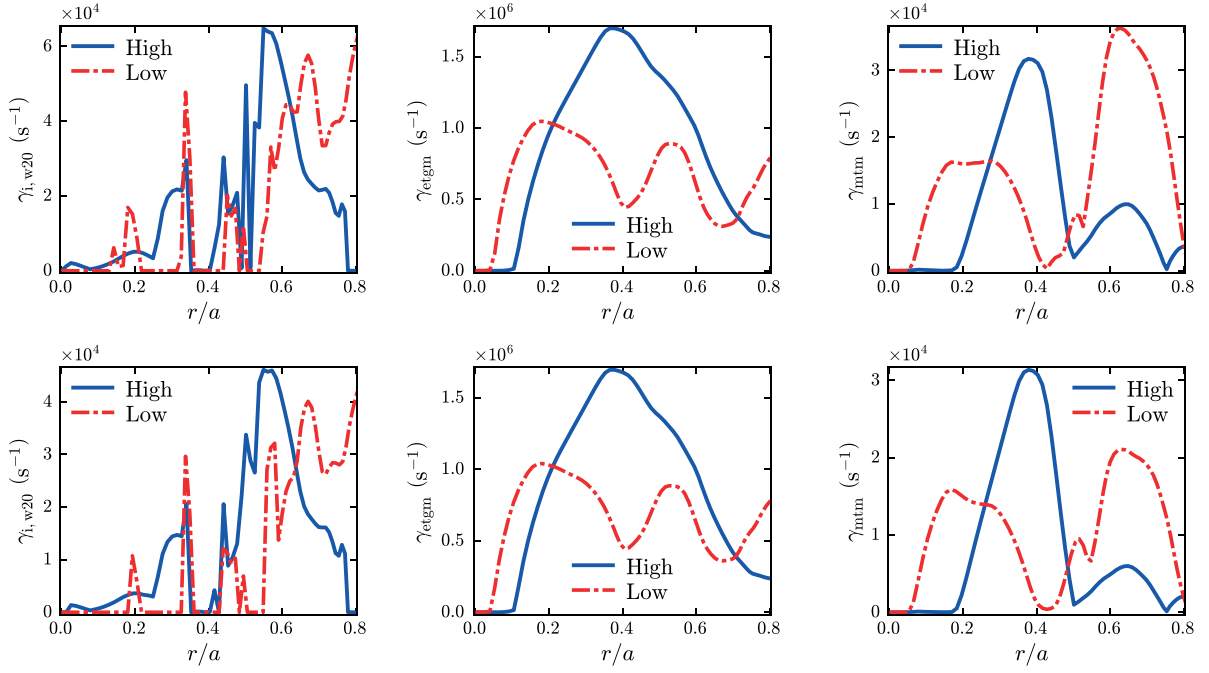


Figure 7. ITG/TEM/KBM growth rate ($\gamma_{i,w20}$), ETGM growth rate (γ_{etgm}), and MTM growth rate (γ_{mtm}) are displayed for hydrogen plasma (first row) and tritium plasma (second row) for high and low collisionality discharges.

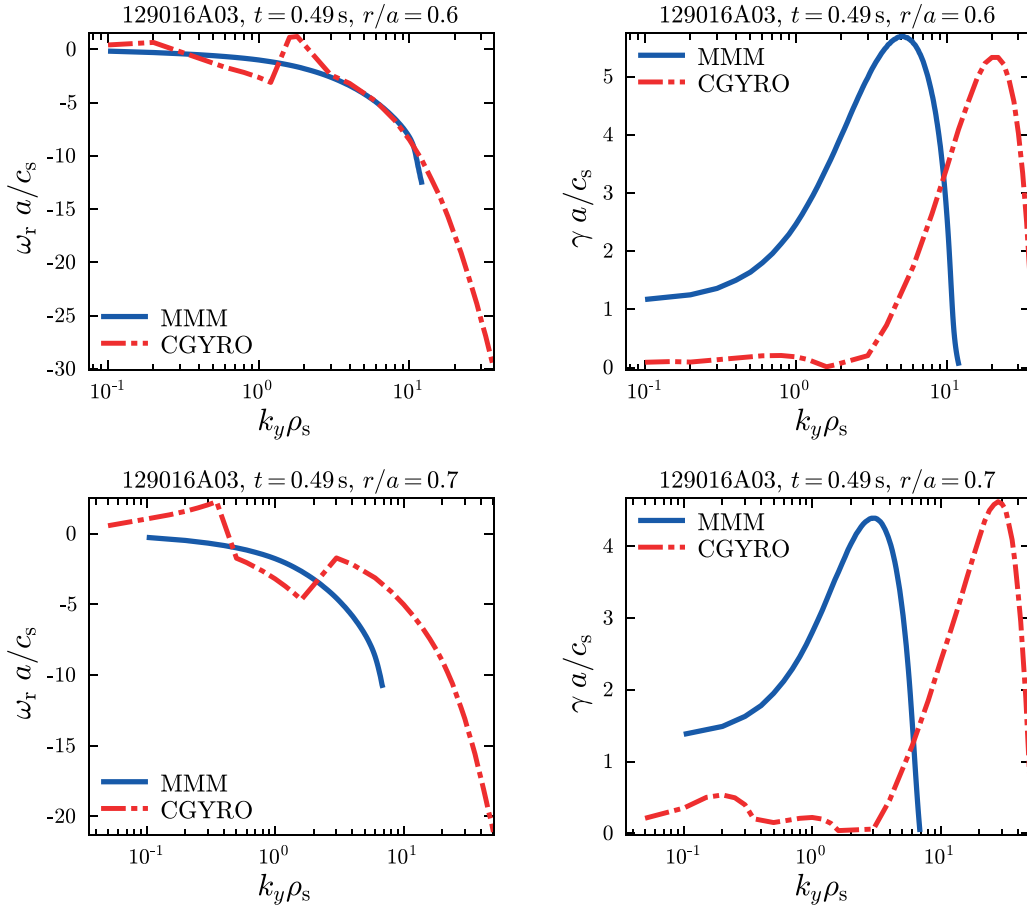


Figure 8. ETG-MMM and ETG-CGYRO normalized real frequency ($\omega_r a/c_s$) and growth rate ($\gamma a/c_s$) for a low collisionality discharge at $r/a = 0.6$ and $r/a = 0.7$.

diffusivity are derived from solutions obtained from each of the four final ETGM model equations: electron continuity, charge conservation, electron momentum, and electron energy equations (equations (3), (5), (7) and (10) in [6]). We further assess the total electron power across the flux surface using the ETG-MMM model and compare it to experimental measurements and nonlinear CGYRO simulation results. The ETG-MMM model yields 2.0 MW of thermal power, aligning with experimental data at $r/a = 0.6$. In contrast, the CGYRO code yields 3.5 MW of thermal power in the nonlinear simulation. However, the ETG-MMM and ETG-CGYRO models both estimate a thermal power of approximately 1.0 MW at $r/a = 0.7$, which is less than the experimental power loss of 2.80 MW. This discrepancy arises most likely from the electron thermal loss caused by the instability of the MTM at that radial position. Neither the CGYRO nor the MMM simulations account for this instability [13]. It is worth noting that the ETG-MMM model exhibits computational efficiency, requiring only approximately 5.0 ms of computation time on a standard desktop. In contrast, nonlinear CGYRO simulations demand 8.0 h on 8 K cores.

5. Comparison of predicted temperatures with experimental data

The updated MMM model version 9.0.4, as implemented in the integrated modeling code TRANSP [2], enables the simulation of electron and ion temperature profiles in NSTX discharges with varying collisionality. The validation study employs integrated modeling simulations, utilizing the numerical PT-SOLVER in the TRANSP code and incorporating NSTX experimental boundary and initial conditions. Equilibrium data is interpolated from the EFIT reconstruction [18]. NBI heating and current drives are acquired through NUBEAM [11]. Neoclassical transport is computed using the Chang-Hinton model [19], and the resistivity and bootstrap current are determined using the Sauter model [20]. The flow shear rate in the MMM is determined using the following strategy:

Waltz *et al* [21] demonstrated that microturbulence suppression occurs when the $\mathbf{E} \times \mathbf{B}$ flow shear rate, denoted as $\omega_{E \times B}$, exceeds the maximum growth rate of all drift modes. This insight has been utilized to simulate the $\mathbf{E} \times \mathbf{B}$ flow shear mechanism in the MMM. This simulation approach employs the reduced growth rate $\gamma - \omega_{E \times B}$ to compute turbulent transport coefficients. Here, γ represents the maximum linear growth rate of the modes in the absence of $\mathbf{E} \times \mathbf{B}$ flow shear. Using this quench rule, $\gamma - \omega_{E \times B}$, turbulence is completely suppressed when $\omega_{E \times B}$ exceeds γ . The flow shear rate integrated into the MMM was originally formulated by Hahn and Burrell [22] for general toroidal geometry as:

$$\omega_{E \times B} = \frac{(RB_{\text{pol}})^2}{B_{\text{tor}}} \frac{\partial}{\partial r} \left(\frac{E_r}{RB_{\text{pol}}} \right). \quad (1)$$

In equation (1), E_r represents the radial electric field, R is the major radius, r is the midplane minor radius, q is the magnetic safety factor, and B_{tor} and B_{pol} denote the toroidal and poloidal magnetic fields, respectively.

The radial electric field E_r is determined using the ion force balance equation:

$$E_r = \frac{\partial p_i / \partial r}{Z_i e n_i} - v_{\text{pol},i} B_{\text{tor}} + v_{\text{tor},i} B_{\text{pol}}, \quad (2)$$

where p_i is the ion pressure, Z_i is the ion charge number, e is the elementary charge, and n_i is the ion density. The three distinct terms in equation (2) account for the effects of diamagnetic drift, poloidal ion velocity ($v_{\text{pol},i}$), and toroidal ion velocity ($v_{\text{tor},i}$). The $v_{\text{tor},i}$ is computed using the NUBEAM module [11], while the $v_{\text{pol},i}$ is computed using the NCLASS neoclassical module [23].

The simulated electron and ion temperatures versus normalized radial location $\hat{\rho}$ are then compared to the corresponding experimental profiles. Notably, the MMM model demonstrates excellent agreement between predicted profiles and experimental data, for high and low collisionality discharges, as shown in figure 9. The ion and electron thermal diffusivities are also presented. Anomalous electron transport is observed, while ion transport is predominantly neoclassical. An exception is noted around $\hat{\rho} = 0.45$, where some anomalous ion transport due to the TE mode is observed in the high collisionality case.

While not all temperature predictions for NSTX discharges by MMM demonstrate outstanding results, they consistently remain within 20% of the root mean square deviation of the experimental data, well within the margin of temperature measurement error. In figure 10, it becomes evident that the MMM exhibits an overprediction of electron temperature at the center. This discrepancy points to an underestimation of electron thermal diffusivity by the MMM. It is clear that there is an additional instability contributing to electron thermal transport, which is not considered in the MMM. In the latest NSTX study using the Trapped Gyro Landau Fluid (TGLF) model [16], predicted temperature profiles were compared to experimental data. While statistically consistent, the numerical results show sensitivity to input parameters, resulting in RMS errors ranging from 6% to 50% depending on simulation setup [24]. It is worth mentioning that a large-scale validation exercise was recently conducted to demonstrate the ability of MMM to reproduce a wide range of conventional tokamak discharges from EAST, KSTAR, JET, and DIII-D [3]. In this validation study for MMM, the average RMS deviation was 9.3% for predicted electron temperature and 10.5% for ion temperature.

MMM's versatility extends to the prediction of profiles for temperature, electron density, current density, and rotation in both existing experiments and future thermonuclear fusion devices. Its exceptional computational efficiency is a critical asset, enabling various applications, including real-time control, tokamak scenario optimization, and uncertainty quantification of experimental data.

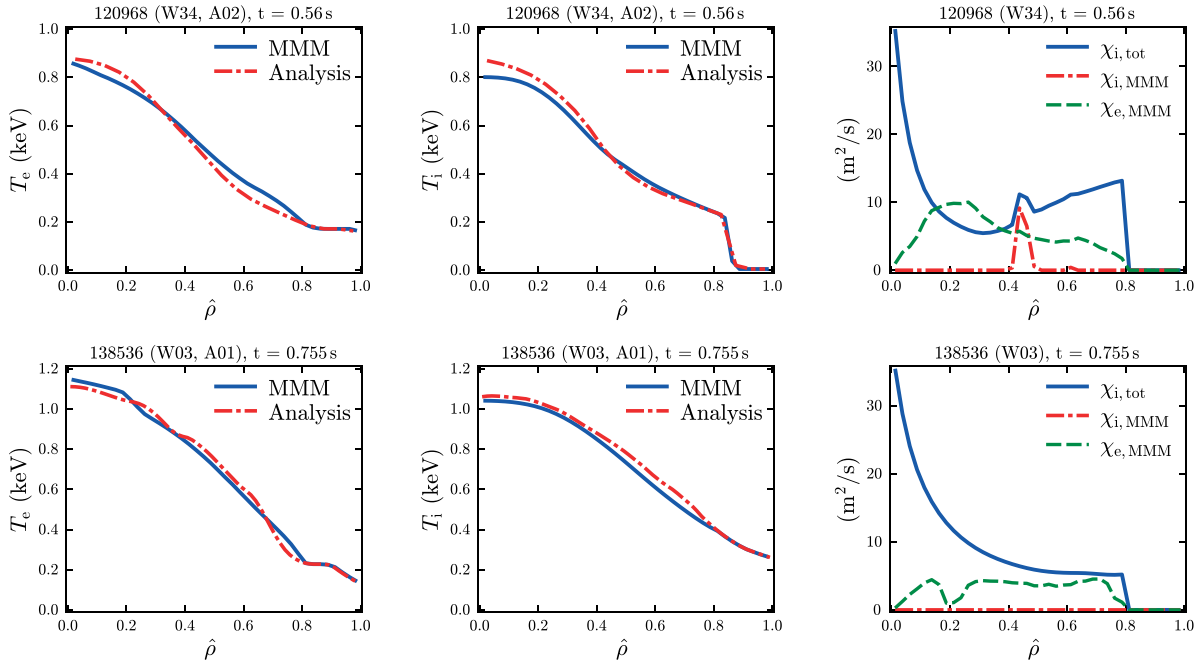


Figure 9. Predicted (MMM) and analysis (experimental) electron and ion temperature profiles, total ion thermal diffusivity ($\chi_{i,tot} = \chi_{neo} + \chi_{i,MMM}$), ion and electron thermal MMM diffusivities ($\chi_{i,MMM}$, $\chi_{e,MMM}$) and ion neoclassical diffusivity (χ_{neo}) for the high collisionality discharge 120968 at $t = 0.56$ s and for the low collisionality discharge 138536 at $t = 0.75$ s.

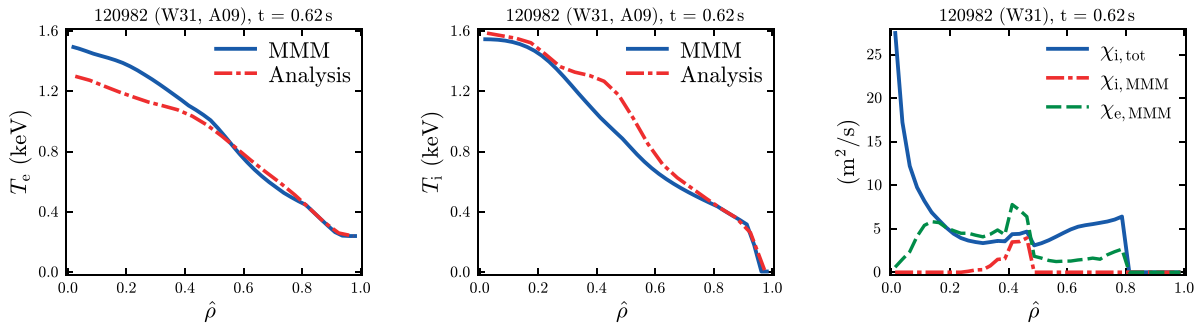


Figure 10. Predicted (MMM) and analysis (experimental) electron and ion temperature profiles, total ion thermal diffusivity ($\chi_{i,tot} = \chi_{neo} + \chi_{i,MMM}$), ion and electron thermal MMM diffusivities ($\chi_{i,MMM}$, $\chi_{e,MMM}$) and ion neoclassical diffusivity (χ_{neo}) for the low collisionality discharge (120982) at $t = 0.62$ s.

6. Conclusions

The research aims to validate the reliability and predictive capability of the MMM in NSTX discharges through the use of the TRANSP code. The demonstration of consistent prediction of electron and ion temperature profiles in low aspect ratio and high beta NSTX discharges is accomplished by first comparing MMM results with gyrokinetic simulations. MMM simulations, encompassing various modes like ITGM, TEM, KBM, PBM, DRIBM, MHD, MTM, and ETGM, reveal stability in all modes except MTM and ETGM within the studied region ($0 < \hat{\rho} \leq 0.8$), aligning with recent gyrokinetic findings. MMM predicts significant electron thermal diffusivity

while attributing almost zero ion thermal diffusivity, indicative of anomalous electron and neoclassical ion thermal transport in NSTX, in agreement with experiments. The stabilizing effects of higher mass isotopes for ITG/TEM/KBM, MTM, and DRIBM are evident, while ETGM shows negligible isotopic influence. Incorporating ion viscosity into MMM is crucial for matching the observed trend of decreasing transport with increasing ion mass. The calculated growth rate and frequency of MTM and ETGM in MMM closely agree with gyrokinetic simulations, highlighting the model's reliability. Furthermore, MMM's computational efficiency is emphasized, making it suitable for various applications, including plasma control and uncertainty quantification in fusion stud-

ies. This study enhances the credibility of MMM, emphasizing its robustness in describing and predicting plasma behavior in NSTX and related fusion research.


Data availability statement

The data that supports the findings of this study is openly available at <https://doi.org/10.34770/fkqv-1h59>.

Acknowledgments

This material is based upon work supported by the U.S. Department of Energy, Office of Science, Office of Fusion Energy Sciences, under Award Numbers DE-SC0013977, DE-SC0021385 and DE-AC02-09CH11466.

ORCID iDs

T. Rafiq  <https://orcid.org/0000-0002-2164-1582>
 C. Wilson  <https://orcid.org/0000-0001-9389-7846>
 C. Clauser  <https://orcid.org/0000-0002-2597-5061>
 E. Schuster  <https://orcid.org/0000-0001-7703-6771>
 J. Weiland  <https://orcid.org/0000-0002-5349-6025>
 J. Anderson  <https://orcid.org/0000-0001-7524-0314>
 S.M. Kaye  <https://orcid.org/0000-0002-2514-1163>
 R.E. Bell  <https://orcid.org/0000-0001-9544-498X>

References

- [1] Rafiq T., Kritz A.H., Weiland J., Pankin A.Y. and Luo L. 2013 *Phys. Plasmas* **20** 032506
- [2] Breslau J. et al 2018 Transp [Computer Software] (<https://doi.org/10.11578/dc.20180627.4>)
- [3] Rafiq T., Wang Z., Morosohk S., Schuster E., Weiland J., Choi W. and Kim H.-T. 2023 *Plasma* **6** 435
- [4] Berkery J.W. et al 2024 *Nucl. Fusion* submitted (<https://doi.org/10.1088/1741-4326/ad3092>)
- [5] Weiland J. 2012 *Stability and Transport in Magnetic Confinement Systems* (Springer)
- [6] Rafiq T., Wilson C., Luo L., Weiland J., Schuster E., Pankin A.Y., Guttenfelder W. and Kaye S. 2022 *Phys. Plasmas* **29** 092503
- [7] Rafiq T., Weiland J., Kritz A.H., Luo L. and Pankin A.Y. 2016 *Phys. Plasmas* **23** 062507
- [8] Rafiq T., Bateman G., Kritz A.H. and Pankin A.Y. 2010 *Phys. Plasmas* **17** 082511
- [9] Weiland J., Rafiq T. and Schuster E. 2023 *Phys. Plasmas* **30** 042517
- [10] Clauser C.F., Guttenfelder W., Rafiq T. and Schuster E. 2022 *Phys. Plasmas* **29** 102303
- [11] Pankin A., Mccune D., Andre R., Bateman G. and Kritz A. 2004 *Comput. Phys. Commun.* **159** 157
- [12] Candy J., Belli E. and Bravenec R. 2016 *J. Comput. Phys.* **324** 73
- [13] Clauser C.F. et al 2023 Studies of ETG transport on NSTX plasmas with gyrokinetics and reduced transport models *29th IAEA Fusion Energy Conf. (FEC 2023) (London, United Kingdom, 16–21 October 2023)* pp 1–25 (available at: <https://www.iaea.org/events/fec2023>)
- [14] Ma J., Wang G., Weiland J., Rafiq T. and Kritz A.H. 2015 *Phys. Plasmas* **22** 012304
- [15] Weiland J., Rafiq T. and Schuster E. 2024 *J. Phys. Plasmas* submitted
- [16] Staebler G.M., Kinsey J.E. and Waltz R.E. 2005 *Phys. Plasmas* **12** 102508
- [17] Rafiq T., Kaye S., Guttenfelder W., Weiland J., Schuster E., Anderson J. and Luo L. 2021 *Phys. Plasmas* **28** 022504
- [18] Lao L., John H.S., Stambaugh R., Kellman A. and Pfeiffer W. 1985 *Nucl. Fusion* **25** 1611
- [19] Chang C.S. and Hinton F.L. 1986 *Phys. Fluids* **29** 3314
- [20] Sauter O., Angioni C. and Lin-Liu Y.R. 1999 *Phys. Plasmas* **6** 2834
- [21] Waltz R.E., Kerbel G.D. and Milovich J. 1994 *Phys. Plasmas* **1** 2229
- [22] Hahn T.S. and Burrell K.H. 1995 *Phys. Plasmas* **2** 1648
- [23] Houlberg W.A., Shaing K.C., Hirshman S.P. and Zarnstorff M.C. 1997 *Phys. Plasmas* **4** 3230
- [24] Avdeeva G. et al 2023 *Nucl. Fusion* **63** 126020